PNAS RESEARCH ARTICLE | CELL BIOLOGY

Length control emerges from cytoskeletal network geometry

Shane G. McInally[a,1], Alexander J. B. Reading[b], Aldric Rosario[c], Predrag R. Jelenkovic[d], Bruce L. Goode[b], and Jane Kondev[c]

Edited by Andrew Murray, Harvard University, Cambridge, MA; received January 26, 2024; accepted June 21, 2024

Many cytoskeletal networks consist of individual filaments that are organized into elaborate higher-order structures. While it is appreciated that the size and architecture of these networks are critical for their biological functions, much of the work investigating control over their assembly has focused on mechanisms that regulate the turnover of individual filaments through size-dependent feedback. Here, we propose a very different, feedback-independent mechanism to explain how yeast cells control the length of their actin cables. Our findings, supported by quantitative cell imaging and mathematical modeling, indicate that actin cable length control is an emergent property that arises from the cross-linked and bundled organization of the filaments within the cable. Using this model, we further dissect the mechanisms that allow cables to grow longer in larger cells and propose that cell length–dependent tuning of formin activity allows cells to scale cable length with cell length. This mechanism is a significant departure from prior models of cytoskeletal filament length control and presents a different paradigm to consider how cells control the size, shape, and dynamics of higher-order cytoskeletal structures.

cytoskeleton | size control | biological scaling | emergence

Significance

Cells control the sizes of their cytoskeletal networks to ensure that these structures can efficiently perform their cellular functions. Until now, this ability has been attributed to molecular feedback mechanisms that control the rates at which individual filaments are assembled and disassembled. We find that size control of cytoskeletal networks does not require this type of feedback and can instead be encoded through the physical arrangement of the filaments within that network. These findings have important implications for understanding how the underlying geometry of higher-order cytoskeletal networks contributes to cellular control over these structures.

Cells possess the remarkable ability to control the size, shape, and dynamics of their intracellular parts (1–3). This behavior is important for promoting proper organelle function and has been observed for many membrane-bound and cytoskeletal organelles found in diverse eukaryotic cells. Further, this suggests that the ability of a cell to govern the geometric properties of its intracellular structures is a fundamental property of living systems.

Cytoskeletal filaments are popular and convenient models used to study the mechanisms that control the size of intracellular structures because their size can be represented by a single dimension, their length. Regardless of their molecular composition (e.g., actin or tubulin), these polymers grow by the addition of molecular building blocks and shrink by their removal. Thus, experimental and theoretical studies of length control aim to identify the nature of the feedback that controls the rates of subunit addition and removal, which allows these filaments to be assembled and maintained at a steady-state length (4). Different mechanisms have been proposed to explain how cytoskeletal structures (e.g., mitotic spindles, cilia, and actin cables) are assembled and maintained at defined lengths, including limiting-pool models, balance-point models, molecular rulers, antenna models, and concentration gradients (5–11). While each of these mechanisms involves distinct molecular details, they all require a control mechanism that tunes the assembly rate, the disassembly rate, or both rates in a length-dependent manner. While this level of abstraction is suitable for individual cytoskeletal filaments, it is unclear how well these types of models explain size control of the many higher-order cytoskeletal structures found in cells.

Cytoskeletal networks found in nature are typically composed of many individual filaments that are organized into higher-order structures with defined architecture and geometry. The specific architectures of these larger, composite structures are crucial for their biological functions (e.g., phagocytosis, cell motility, and pathogenesis), yet much of the work investigating how these structures are assembled and regulated has focused on the mechanisms that control the turnover of individual filaments. To gain a better understanding of how these higher-order structures are controlled by the cell, we need to consider how the geometric arrangement of filaments within these structures contributes to emergent properties of these higher-order networks.

Here, we address this question using yeast actin cables as a model. Each actin cable in a yeast cell is a bundle composed of many short, overlapping actin filaments polymerized by formins (12). In the budding yeast *Saccharomyces cerevisiae*, cables are assembled by two genetically redundant formins, which localize during bud growth to the bud tip (Bni1) and bud neck (Bnr1) (13–15). The cables polymerized by Bni1 and Bnr1 are polarized structures, with their barbed ends oriented toward the bud tip and neck, respectively. This property enables them to serve as railways for essential myosin-based transport of secretory vesicles and organelles to the growing bud cell (12, 16). It is thought that controlling actin

Author affiliations: [a]Department of Biology and Biotechnology, Worcester Polytechnic Institute, Worcester, MA 01609; [b]Department of Biology, Brandeis University, Waltham, MA 02454; [c]Department of Physics, Brandeis University, Waltham, MA 02454; and [d]Department of Electrical Engineering, Columbia University, New York, NY 10027

Author contributions: S.G.M., B.L.G., and J.K. designed research; S.G.M., A.J.B.R., A.R., P.R.J., and J.K. performed research; S.G.M. contributed new reagents/analytic tools; S.G.M., A.J.B.R., and A.R. analyzed data; and S.G.M. wrote the paper.

The authors declare no competing interest.

This article is a PNAS Direct Submission.

[1]To whom correspondence may be addressed. Email: smcinally@wpi.edu.

This article contains supporting information online at https://www.pnas.org/lookup/suppl/doi:10.1073/pnas.2401816121/-/DCSupplemental.

Published August 6, 2024.

cable length promotes efficient intracellular transport and therefore polarized growth in these cells (9, 17–19). In support of this hypothesis, we have recently shown that yeast actin cables grow so that their length closely matches the length of the mother cell in which they are assembled (20). We found that the scaling of cable length with cell length is conferred through control over their assembly—initially cables grow fast, but as they grow longer and approach the back of the cell their rate of growth steadily slows down or decelerates. Ultimately, cable growth stops when the length of the cable matches the length of the cell. In addition, we showed that this cable deceleration behavior was different in smaller versus larger cells. This suggests that cable growth is tuned in a cell length–dependent manner, but the underlying mechanism has remained unclear.

Here, we present a mathematical model that explores how the specific architecture of a cable can enable length control. This model for cytoskeletal length control is a significant departure from previous length control models because there is no length-dependent molecular feedback mechanism that tunes the rates of assembly or disassembly. Instead, the control over cable length naturally emerges from the geometric arrangement of the filaments within the network.

Results

Actin Cables Undergo Length-Dependent Tapering. To date, our models of actin cable length control have treated cables as one-dimensional, linear structures with a single barbed end at which actin monomers are added, and a single pointed end at which actin monomers are removed (9, 19, 20). This approach was inspired by models of length control for other types of cytoskeletal structures, most notably for microtubule-based flagella (21). However, it has been shown that cables are composed of many shorter, overlapping actin filaments bundled together by actin cross-linkers (22). Therefore, we were interested in determining whether the architecture of the cable could provide insights into how its length is controlled (23–25).

We started by asking whether the width of cables is uniform along their lengths. To address this, we fixed and stained wild-type haploid budding yeast cells with fluorescently labeled phalloidin and imaged them using superresolution microscopy. From these images, we traced the entire length of the cables that could be clearly tracked in mother cells (i.e., those that do not intersect with other cables or actin patches) from their origin at the bud neck to their terminal end in the mother cell (Fig. 1*A*). We measured the fluorescence intensity along the entire length of the cable and took this to be proportional to cable width or thickness. We found that cable width was not uniform, but instead tapers as cables get longer (Fig. 1*B*). Specifically, cables were thicker in the region closest to the bud neck, where formin-mediated cable assembly takes place, and their thickness progressively decreased along their length. Further, the cable tapering profile was well fit by a single exponential with a decay length of 1.54 ± 0.08 μm (all reported values represent mean ± 95% CI, unless otherwise indicated).

Two-Dimensional Model of Cable Length Control. The tapering of actin cable thickness was reminiscent of tapering previously reported for other types of actin networks (e.g., *Listeria* comet tails and fish keratocyte lamellipodial fragments) (26–28). This prompted us to consider whether related mechanisms may explain how the structure and length of actin cables are regulated. To test this idea, we developed a mathematical model of cable length control (Fig. 1*C*), in which multiple formin molecules (N_f) are

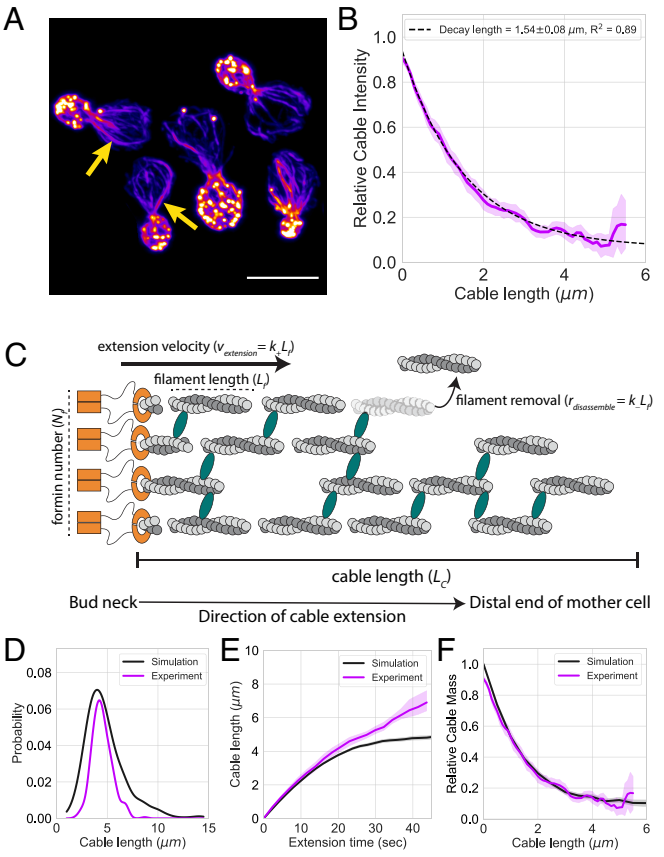

Fig. 1. Two-dimensional model of cable length control. (*A*) Representative maximum intensity projection images of haploid yeast cells fixed and stained with labeled phalloidin. Arrows indicate single actin cables that clearly display their tapered shape. (Scale bar, 5 μm.) (*B*) Relative actin cable fluorescence intensity measured in three independent experiments. Solid magenta line and shading, mean and 95% CI for all three experiments (n = 47 cables). Tapering profile decay length (±95% CI) was determined by fitting the profile to a single exponential. (*C*) Schematic of the two-dimensional model of actin cable length control. Multiple formins (orange, N_f) simultaneously assemble short actin filaments with a characteristic length (L_f) at a constant rate (k_+). These filaments are cross-linked and bundled (green ellipses) with neighboring filaments to form the cable and continue to extend into the cell at the same rate at which filaments are assembled by formins ($v_{extension} = k_+L_f$). Each filament has an independent probability of being removed ($r_{disassemble} = k_-L_f$) from the cable. Thus, the length of the cable (L_c) is the distance from the site of assembly to the distal tip of the longest surviving filament in the cable. (*D*–*F*) Results obtained from simulations (black lines) compared with experimental measurements (magenta lines) of cable length (*D*), cable extension rate (*E*), and cable tapering (*F*). The parameters used for these 500 independent simulations were k_+ = 0.50 s^{-1}, k_- = 0.16 s^{-1}, L_f = 500 nm, and N_f = 4 formins. Solid lines and shading indicate mean and 95% CI, respectively.

localized at the bud neck and produce actin filaments of a fixed length (L_f) at a constant rate (k_+). As these filaments are assembled, they are incorporated into the cable bundle by cross-linkers. As a result of polymerization and cross-linking, the entire bundle collectively grows as a single unit, extending into the mother cell at a constant velocity ($v_{extension} = k_+L_f$), which is equivalent to the number of actin monomers that are added to the growing cable by formins at the bud neck. Once incorporated into the growing bundle, each filament has an independent probability of being targeted for removal through an unspecified disassembly mechanism. Because each of these filaments has a fixed length (L_f), the speed at which monomers are removed from the cable is constant ($r_{disassemble} = k_-L_f$). Thus, the entire length of a cable (L_c) is equal to the distance between its site of assembly (the bud neck) and its distal end, defined by the last surviving filament within the bundle. Importantly, none of these parameters have

an inherent length dependence, and therefore, all parameters in this model are constants.

To derive estimates for the parameters in our model, we referred to our prior study of cable length control (20), in which we determined that the average length of cables in haploid budding yeast was 4.48 ± 0.98 μm. We also used linear regression to measure the extension velocity of cables (i.e., the slope of the initial linear phase of cable growth) from our prior measurements of cable extension rates in haploid cells ($v_{extension} = 0.25 \pm 0.02$ μm/s, *SI Appendix*, Fig. S1*A*). To estimate the remaining unmeasured parameters in our model, we used the following mathematical relationship that describes the mean length of a bundle of filaments:

$$< L_c > \; = \lambda \left(\gamma + \ln \left(\frac{k_+}{k_-} N_f \right) \right), \qquad [1]$$

where $< L_c >$ is the mean cable length, $\gamma \approx 0.577$ (i.e., the Euler-Mascheroni constant), and N_f is the number of formins assembling a single actin cable; for derivation see *SI Appendix*. Importantly, λ is the cable tapering profile in Fig. 1*B*, and can be related to the model parameters through the decay constant, defined as

$$\lambda = \frac{k_+}{k_-} L_f. \qquad [2]$$

Using Eq. **2** with our measurements of the extension velocity ($v_{extension}$) and the tapering decay profile (λ), we estimate $k_- = 0.16 \pm 0.01$ s^{-1} (mean ± SD).

While we were unable to compute N_f and L_f without direct measurements of at least one of these parameters, a prior electron microscopy study of actin cables in *Schizosaccharomyces pombe* found that the average length of these filaments was 0.49 ± 0.26 μm (mean ± SD) (22). We used these measurements to estimate $L_f \sim 0.5$ μm and, with Eq. **1**, estimate that four formins ($N_f \sim 4$ formins) cooperate to assemble a single cable.

Next, we conducted computational simulations using the parameters estimated above ($k_+ = 0.50$ s^{-1}, $k_- = 0.16$ s^{-1}, $L_f = 500$ nm, $N_f = 4$ formins) and found that this model can assemble actin cables that resemble those observed in vivo. Remarkably, our model produced cables that exhibit a peaked distribution of lengths, decelerated growth, and tapered actin profiles (Fig. 1 *D*–*F*, black lines), despite the absence of any length-dependent parameters. Next, we directly compared the results of these simulations with our experimental measurements (Fig. 1 *D*–*F*, magenta lines) and found that this model can adequately recapitulate our experimental data without the use of any fitted parameters. We further validated our simulations by comparing these results with the analytical solutions for each of these cable behaviors (*SI Appendix*, Fig. S2 *A*–*C*).

Cable Extension Velocity Is Independent of Cell Size. Next, we wanted to determine which parameters in our model may be tuned in a cell length–dependent manner to permit the previously observed scaling of cable length with cell length (20). First, we considered whether the extension velocity may be cell length-dependent. To determine how extension velocity changes as a function of cell size we referred to our prior quantification of cable extension rates from temperature-sensitive *cdc28-13^{ts}* cells. At the permissive temperature, *cdc28-13^{ts}* cells are similar in size to wild-type haploid budding yeast; however, their size increases when grown at the nonpermissive temperature (20, 29, 30). In our prior study, we quantified cable extension rates from these enlarged cells by tracking the tips of cables marked with the fluorescent cable reporter Abp140-GFP^{Envy}. Here, we reanalyzed these measurements by using linear regression to compare the extension velocity (i.e., the slope of the initial linear phase of actin cable growth) in induced and uninduced *cdc28-13^{ts}* cells. We found that despite the nearly twofold difference in cell length, the initial extension velocity was not significantly different ($v_{extension,uninduced} = 0.22 \pm 0.02$ μm/s, $v_{extension,induced} = 0.24 \pm 0.02$ μm/s; $P = 0.23$) (*SI Appendix*, Fig. S1*B*). Thus, the initial extension velocity of cables is independent of cell size and does not likely contribute to the scaling of cable length with cell length.

The Amount of Formin at the Bud Neck Scales with Cell Length. Next, we considered whether differences in the amount of formin molecules (Bnr1) or their spatial organization at the bud neck might contribute to the scaling of cable length with cell length. To determine whether the amount of Bnr1 at the bud neck changes in cells of different sizes, we tagged Bnr1 with GFP^{Envy} and Cdc3 (a component of the septin collar at the bud neck) with mCherry in *cdc28-13^{ts}* cells (Fig. 2*A*). We grew the cells for 0, 4, or 8 h at the nonpermissive temperature to induce different changes in cell size and then returned cells to the permissive temperature to allow polarized growth for 1 h. Next, we mixed approximately equal numbers of cells of the three different sizes and performed live imaging on the cell populations using spinning disk confocal microscopy. We used the Cdc3-mCherry signal to generate segmentation masks of the bud neck and within this mask measured the total fluorescence intensity of Bnr1-GFP^{Envy} at the bud neck. From the same images, we also measured the distance from the bud neck to the rear of the mother cell (i.e., cell length).

To determine whether the amount of Bnr1-GFP^{Envy} at the bud neck changes as a function of cell length, we analyzed the data on a double logarithmic plot, which revealed a linear scaling relation between the amount of Bnr1 at the bud neck and cell length (Fig. 2*B*). To determine the nature of this scaling relation, we fit the data using the power law ($y = Ax^a$), where a is the scaling exponent that describes the relationship between the two measured quantities, cell length and Bnr1-GFP^{Envy} intensity (3). We found that the scaling exponent was slightly hyperallometric ($a_{formin} = 1.25 \pm 0.12, R^2 = 0.49$), indicating that a greater amount of formin was localized to the bud neck in larger cells compared to smaller cells.

The Number of Actin Cables in the Mother Cell Scales with Cell Length. Our observations above prompted us to next ask whether larger cells, which have higher levels of Bnr1 at the bud neck, might assemble thicker cables and/or an increased number of cables. To quantify the number of cables in the mother cell compartment of cells of different sizes, we used line scans drawn across the equator of haploid, diploid, and *cdc28-13^{ts}* temperature-sensitive cells fixed and stained with fluorescently labeled phalloidin (Fig. 2*C*). Diploid yeast cells have ~twofold increase in volume compared to haploid cells, and *cdc28-13^{ts}* cells grown at the nonpermissive temperature for 8 h have a ~fivefold increase in cell volume (20, 31). Next, we used automated fluorescent peak detection from the line scans to quantify the number of cables in the mother cell compartment (Fig. 2*D*). We also measured the length of the mother cell (i.e., the distance from the bud neck to the rear of the mother cell) in each cell.

We found that the mean number of cables was 9 ± 2 in haploid cells and 13 ± 3 in diploid cells. Additionally, the mean number of cables in *cdc28-13^{ts}* cells grown at the permissive temperature was 7 ± 2, while the mean number of cables in *cdc28-13^{ts}* cells grown at the restrictive temperature was 16 ± 3 (Fig. 2*E*). We performed a power law analysis to compare how the number of

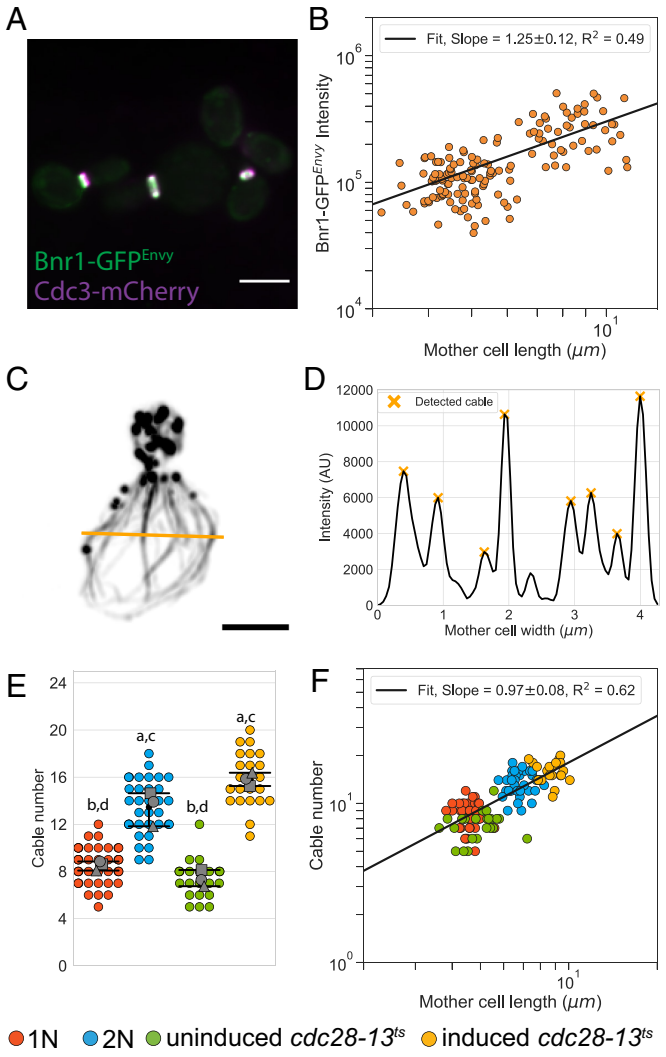

Fig. 2. The amount of Bnr1 formin at the bud neck and the number of actin cables in a cell scale with cell length. (*A*) Representative maximum intensity projection image of *cdc28-13*^{ts} cells grown to different sizes while expressing fluorescently labeled Bnr1 (Bnr1-GFP^{Envy}) and Cdc3 (Cdc3-mCherry). (Scale bar, 5 μm.) (*B*) Amount of Bnr1-GFP^{Envy} localized to the bud neck of *cdc28-13*^{ts} cells grown to different sizes plotted against mother cell length on a double logarithmic plot and fit using the power law. Bnr1-GFP^{Envy} was measured in three independent experiments (n = 148 cells). (*C*) Representative maximum intensity projection images of a haploid yeast cell fixed and stained with labeled phalloidin. (Scale bar, 2 μm.) The yellow bar indicates the ROI position used to generate the line scan profile (*D*) used for automated peak detection (orange X's indicate detected actin cables). (*E*) The number of actin cables measured from haploid (red), diploid (blue), uninduced *cdc28-13*^{ts} (green), and induced *cdc28-13*^{ts} (yellow) cells fixed and stained with labeled phalloidin. Each data point represents an individual cell. Larger symbols represent the mean from each of the three independent experiments (n = 119 cells). Error bars indicate 95% CI. Statistical significance was determined by Student's *t* test. Significant differences ($P \leq 0.05$) indicated for comparisons with haploid ("a"), diploid ("b"), uninduced cdc28-13ts ("c"), and induced cdc28-13ts ("d"). (*F*) Actin cable number plotted against mother cell length on a double logarithmic plot and fit using the power law.

cables changes as a function of cell size and found that there is an isometric scaling relation $\left(a_{cable\ number} = 0.97 \pm 0.08,\ R^2 = 0.62\right)$ between the number of cables and the length of the cell (Fig. 2*F*).

Actin Cables Taper in a Cell Length–Dependent Manner. Thus far, our data suggest that larger cells have a greater amount of formin molecules localized to their bud neck (i.e., the site of cable assembly); however, instead of using these formins to assemble thicker cables, they assemble more cables. To explicitly test whether cables in larger cells are thicker than those in smaller cells, we compared cable tapering profiles from uninduced and induced *cdc28-13*^{ts} cells, which were fixed and stained with fluorescently labeled phalloidin. To control for possible differences in the efficiency of phalloidin staining between these different samples, we mixed approximately equivalent amounts of uninduced and induced *cdc28-13*^{ts}cells and then simultaneously fixed, stained, and imaged them using superresolution microscopy (Fig. 3*A*). For each cell in the population, we measured the fluorescence intensity along the length of its cables and the length of the mother cell. To distinguish between the uninduced and induced *cdc28-13*^{ts} cells, we used mother cell length to sort cells into bins containing either "small" or "large" cells. To validate this binning strategy, we plotted the cable lengths we measured from these cells and found that the mean cable length in each bin was consistent with our previous measurements $(L_{cable,small} = 4.1 \pm 0.3\ \mu m, L_{cable,large} = 7.3 \pm 0.8\ \mu m)$ (Fig. 3*B*) (20).

We first compared the cable fluorescence intensity at the region closest to the bud neck (i.e., the region where new filaments are added to the cable) to determine whether the cables in larger cells were thicker than those in smaller cells. We found that while initial cable thickness was more variable in larger cells than smaller cells, there was no statistically significant difference between these bins (Fig. 3*C*). These findings indicate that the number of formins incorporating new actin filaments into a single cable is similar in cells of different sizes and therefore does not contribute to the scaling of cable length with cell length.

We next wanted to determine whether differences in how filaments are removed from the cable bundle may contribute to the scaling of cable length with cell length. To test this, we measured the decay length (λ) from the actin tapering profiles for each bin, as this measurement directly reflects the rates at which filaments are added and removed from the bundle (Eq. **2**). Comparing the decay length (λ) from the actin tapering profiles for each bin revealed that the decay length was ~twofold greater in larger compared to smaller cells $(\lambda_{small} = 1.39 \pm 0.04\ \mu m,\ \lambda_{large} = 2.79 \pm 0.06\ \mu m)$ (Fig. 3*E*). We also noted that the ratio of decay lengths between bins was similar to the ratio of average cell length between bins $(L_{cell,large}/L_{cell,small} = 2.0 \pm 0.3, \lambda_{large}/\lambda_{small} = 2.0 \pm 0.1)$ (Fig. 3*D*). To determine whether these actin tapering profiles were cell length-dependent, we normalized cable length by the length of the cell in which it was measured and then measured the decay lengths from these normalized profiles. Upon normalization, the actin tapering profiles collapse to a single profile with indistinguishable decay lengths $(\lambda_{norm,small} = 0.31 \pm 0.01, \lambda_{norm,large} = 0.29 \pm 0.01)$ (Fig. 3*F*), indicating that the mechanism that confers actin cable tapering is a cell length–dependent process.

Scaling of Actin Cable Length by Tuning Filament Length. Our observation that cable tapering profiles depend on cell length presents two possible mechanisms by which cells can scale the length of their cables with cell length: They could either tune the length of filaments assembled by formins in a cell length–dependent manner (Fig. 4*A*, Model 1), or they could tune the rate of disassembly in a cell length–dependent manner (Fig. 4*A*, Model 2). To distinguish between these two mechanisms, we compared simulations of these two models with our experimental quantifications of cable length, extension rate, and tapering in smaller and larger cells.

First, we conducted simulations of cable assembly using the parameters we derived above for wild-type haploid cells and compared these results with simulations where the disassembly rate (k_-)

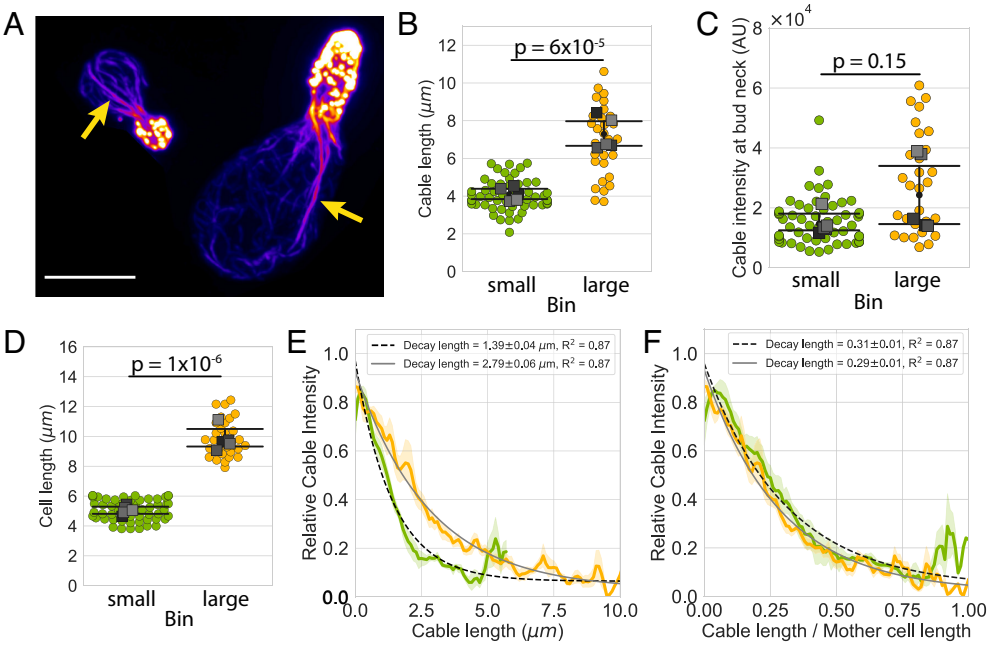

Fig. 3. Actin cable tapering is cell length-dependent. (*A*) Representative maximum intensity projection images of small (*Left*) and large (*Right*) *cdc28-13*^{ts} cells fixed and stained with labeled phalloidin. Arrows indicate single actin cables that clearly display their tapered shape. (Scale bar, 5 μm.) (*B*) Actin cable length and (*C*) actin cable fluorescence intensity in the bud neck region measured from mixed populations of uninduced and induced *cdc28-13*^{ts} cells. Cells were binned based on cell length (*D*); small cells are indicated in green while large cells are indicated in yellow. Each data point represents an individual cable. Larger symbols represent the mean from each experiment. Error bars indicate 95% CI. Statistical significance was determined by Student's *t* test. (*E*) Relative actin cable fluorescence intensity plotted against cable length and (*F*) relative actin cable fluorescence intensity plotted against the ratio of cable length/cell length. Solid lines and shading, mean and 95% CI. Tapering profile decay lengths (±95% CI) were determined by fitting each profile to a single exponential. All data were generated from five independent experiments (n = 84 cables).

had been scaled by cell length. We found that while the decay profiles from these simulations agree with our experimental measurements (*SI Appendix*, Fig. S3*A*), this mechanism was not able to recapitulate our other experimental observations. Specifically, the cables assembled during the simulations of this mechanism were longer than the cables measured in cells ($< L_c >_{large,simulation} = 11.0 \pm 1.0$ μm, $< L_c >_{large,experiment} = 8.2 \pm 0.4$ μm) and the ratio of their lengths was also greater than measured $\left(\frac{< L_c >>_{large,simulation}}{< L_c >>_{small,simulation}} = 2.3 \pm 1.9\right)$ (Fig. 4*D* and *SI Appendix*, Fig. S3 *B–D*). Thus, it appears that tuning the disassembly rate alone cannot explain actin cable length scaling.

Next, we wanted to determine whether our experimental observations are consistent with a mechanism where the length of the filaments assembled by formins are scaled with cell length. Importantly, scaling the length of these filaments with cell length requires that both the rates of filament assembly and disassembly are also scaled in a similar manner. This is due to how these rate constants are defined in our model—each rate constant is defined by the amount of time required to either assemble or disassemble a single filament. In the model, filaments are assembled by formins at a constant extension velocity that is independent of cell size; however, the time that these formins are actively adding monomers to the filaments is scaled proportionally with cell length. Because filament disassembly occurs at a constant rate, the time required to fully disassemble these filaments also scales with cell length. Therefore, a twofold increase in filament length requires twice as much time to assemble that filament and twice as much time to disassemble that filament.

We found that our experimental data closely resemble the results of our simulations of cable assembly where the formins assemble filaments whose lengths are scaled with cell length. Specifically, the mean cable lengths from these simulations were not significantly different from our experimental measurements ($< L_c >_{large,simulation} = 8.7 \pm 0.3$ μm, $< L_c >_{small,simulation} = 4.7 \pm 0.2$ μm), and the ratio of cable lengths between small and large cells was also consistent with our experimental data ($\frac{< L_c >>_{large,simulation}}{< L_c >>_{small,simulation}} = 1.9 \pm 1.1$; Fig. 4 *B–D*) (20). We also found that these simulations closely resemble our measurements of cable tapering (Fig. 4*E*) and cable extension rates measured in small and large *cdc28-13*^{ts} cells (Fig. 4*F*).

To further compare these two models of cable length scaling, we tested their ability to recapitulate our experimentally measured distribution of cable lengths by plotting the empirical cumulative density function for each of the simulations on the same plot as our data (Fig. 4*D*). This visual comparison shows that the model where filament length is scaled with cell length (i.e., Model 1) overlaps more frequently with our data than the model where the disassembly rate is scaled with cell length (i.e., Model 2). We also computed the mean squared error (*MSE*) to directly compare the simulated cable length distributions with our data and found that this quantity was smaller for the filament length scaling model ($MSE = 6.3 \times 10^{-4}$ μm^2) than the disassembly rate scaling model ($MSE = 1.4 \times 10^{-3}$ μm^2), indicating a better fit of the data. These findings are further supported by our analytic calculations (Fig. 4*A* and *SI Appendix*, Fig. S4 *A–C*; for details, see *SI Appendix*). Thus, our experimental measurements are consistent with a mechanism where actin cable length is scaled to match cell length through a process that tunes the lengths of the filaments assembled by formins such that formins in longer cells assemble longer filaments.

Discussion

In this study, we present a feedback-independent model of length control that describes how *S. cerevisiae* controls and scales the length of its actin cables (Fig. 1*C*). This model differs from prior models of length control in that it does not treat each cable as a one-dimensional filament, nor does it assume that any of the model parameters are tuned in a manner that depends on cable length. Instead, our model considers the actual, two-dimensional arrangement of the cross-linked and bundled filaments that compose the cable (Fig. 1*C*). Additionally, all processes that contribute to the assembly and maintenance of the structure (e.g., the rates of filament addition and removal, the number of nucleators) are treated as constants that are independent of the size of the structure being assembled. Despite the absence of feedback, this model recapitulates all known quantitative features of cable length control when two conditions are met: 1) the filaments that compose cables are bundled, and 2) each filament is removed from the

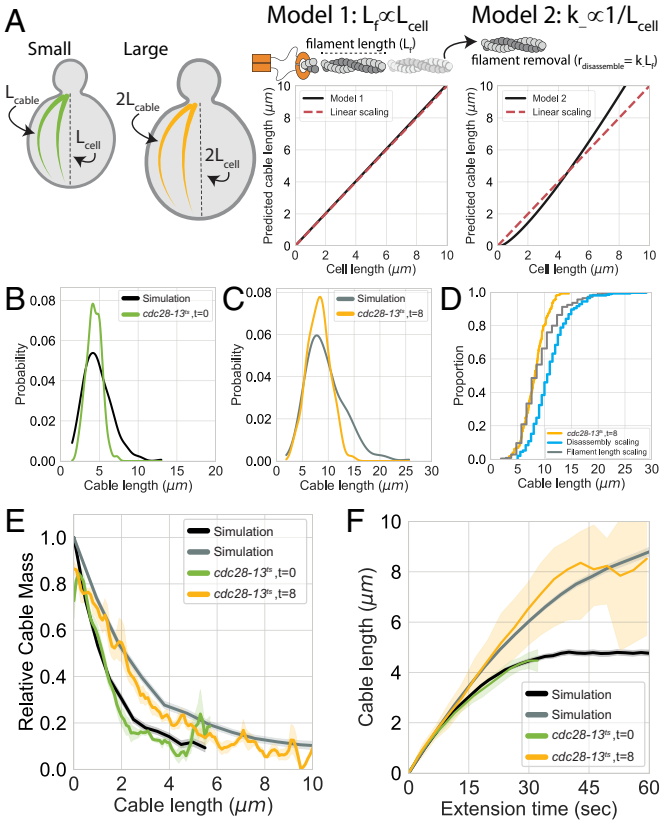

Fig. 4. Tuning the length of formin-generated filaments scales actin cable length with cell length. (*A*) Predicted scaling of cable length with cell length when either filament length (Model 1) or disassembly rate (Model 2) is tuned in a cell length–dependent manner. Black lines indicate theoretical predictions obtained from Eq. **1** where either filament length (*Left*) or disassembly (*Right*) is scaled with cell length. Dashed red lines indicate linear scaling of cable length with cell length. (*B–E*) Comparisons between simulations conducted using the cell size–specific filament lengths (black and gray lines), simulations conducted using cell size–specific disassembly rates (cyan line), and experimentally measured actin cable parameters from uninduced (green lines) and induced *cdc28-13^{ts}* cells (yellow lines). (*B–D*) Comparisons of actin cable length distributions, (*E*) actin cable tapering profiles, and (*F*) actin cable extension rate. Solid lines and shading indicate mean and 95% CI, respectively.

bundle with an independent probability. Thus, rather than relying on size-dependent feedback, control over cable length instead emerges from the geometric arrangement of the shorter filaments that comprise the network.

Due to the minimal number of experimentally accessible parameters that define this model, we were able to use our quantitative experimental measurements to generate predictions for each of the parameters in our model and then test these predictions using computational simulations. We found that our simulations of actin cable assembly using these parameters capture the key quantitative phenotypes displayed by actin cables in vivo—the distribution of cable lengths is peaked, cable extension rate decelerates as the cable grows longer, and cables taper along their length (Fig. 1 *D–F*). While the results of these simulations are very similar to our experimental measurements, we found that there are some notable differences (e.g., the width of the distribution from the simulation is greater than the width of the distribution measured experimentally). These differences between our theoretical and experimental results suggest that while our model adequately describes the mean behavior of cables (e.g., average cable length, extension rate, etc.) there are likely additional mechanisms that further control the assembly and length of actin cables in vivo (32–34). For instance, rather than explicitly considering barbed end capping and filament bundling, we instead take these processes into account implicitly by assuming that monomers are not added to filaments once they are incorporated into the cable bundle and that all filaments within the bundle collectively move as new filaments are added at the site of cable assembly. Additionally, some of these differences may arise due to the complicated nature of performing quantitative experiments on such a highly dynamic cytoskeletal system. We expect that further technological developments that increase the spatial and temporal resolution with which we can observe actin cables in live cells will help to further refine the predictions for the parameters we identify in this study.

We were also interested in testing how the parameters in our model may be tuned in a cell length–dependent manner to confer the scaling of actin cable length with cell length. Our prior work provided a quantitative description of how cables grow to lengths that closely match the length of the cell, however, we could only speculate about possible molecular mechanisms that would confer this behavior (20). Here, we were able use our model of cable length control to computationally and experimentally eliminate potential mechanisms that may confer this scaling behavior.

Actin cables are assembled by two complementary sets of formins, one localized to the bud neck (Bnr1) and one localized to the bud tip (Bni1) (13–15). Our study has focused only on the cables assembled by Bnr1, which assembles and organizes cables that enter the mother cell. Prior studies have shown that Bnr1 colocalizes with components of the septin collar in regularly spaced pillars around the bud neck (35–38). These pillars are thought to serve as sites of actin cable assembly, as actin cables have been observed to emerge from these sites as they grow into the mother cell. Additionally, it has been observed that the diameter of the bud neck scales with cell length through an unknown mechanism (39). Therefore, we sought to determine whether these sites of actin cable assembly are sensitive to changes in cell size in order to assemble longer cables in larger cells.

Our quantitative analyses of how cables are assembled in cells of different sizes revealed that while there is a greater amount of formin (Bnr1) localized to the bud neck in larger cells (Fig. 2*B*), these cables are assembled at the same rate (*SI Appendix*, Fig. S1*B*) and have the same initial thickness as smaller cells (Fig. 3*C*). Additionally, we found that larger cells assemble a greater number of cables when compared with smaller cells (Fig. 2 *E* and *F*). Taken together, these results suggest that the molecular composition and arrangement of formins within these sites of cable assembly are likely cell size independent, but that the number of these assembly sites scales with cell length. Our data also show that the initial cable thickness is more variable in larger cells when compared to smaller cells (Fig. 3*C*). This wider distribution of initial cable thickness in larger cells suggests that there may be a greater heterogeneity in the molecular composition of the formin-septin pillars that nucleate cable assembly. However, due to the weak, logarithmic dependence of cable length on formin number in our model (Eq. **1** and *SI Appendix*, Fig. S4*A*), we do not expect that this contributes to the scaling of cable length with cell length. The mechanisms that control the size, number, and composition of these cable assembly sites are currently unknown, but we suspect that their proper assembly is required to ensure that the flux of growth factors undergoing transport along cables is sufficient to support the growth of the daughter cell.

Our analysis of actin cable tapering profiles from cells of different sizes presented two possible mechanisms to scale actin cable length with cell length—either the rate at which filaments are removed from the cable or the length of the filaments that compose the cable are scaled with cell length. When we compared computational simulations and analytic calculations of each

mechanism with our experimental measurements, we found that our data are highly consistent with a mechanism where the length of the filaments that compose the cable is tuned in a cell length–dependent manner (Fig. 4 and *SI Appendix*). While we have not generated direct experimental evidence to support this mechanism, prior studies have demonstrated that mutants that lack the ability to properly tune formin activity exhibit defects in actin cable length regulation and organization (17–19, 40, 41). Therefore, we suspect that the tuning of filament length may be driven by regulators that either inhibit formin activity (e.g., Smy1 and Hof1) or displace formins from the barbed ends of growing filaments (e.g., Bud14). Furthermore, it is unclear how the activity or abundance of these types of formin regulators is controlled in a cell length–dependent manner.

Generally, protein abundance is thought to scale with cell volume such that their concentration is maintained across variations in cell size (42, 43). However, recent studies have identified small subsets of proteins in cells that deviate from this behavior and either "subscale" or "superscale" with cell volume (30, 44). Therefore, we suspect that regulators of formin activity may exhibit similar scaling behaviors so that their abundance scales with other aspects of cell geometry (e.g., cell length or cell surface area). Alternatively, it has been recently demonstrated that cells can also exploit the different rates at which cell volume and surface area scale to tune the size of their mitotic spindle and nucleus with cell size (45, 46). Thus, it is possible that budding yeast utilize a similar mechanism to tune the activity of formins in a cell length–dependent manner.

Importantly, our model of actin cable length control was inspired by studies investigating the actin cytoskeleton arrays assembled by diverse cell types (e.g., *Listeria* and fish keratocyte lamellipodial fragments) that observed similar actin tapering profiles (27, 28). While these structures provide fundamentally different biological functions (e.g., generating the force required for motility, or serving as tracks for intracellular transport) it appears that much of their behavior is controlled through a simple set of components—nucleators that promote the assembly of filaments, bundling or cross-linking factors that organize filaments into a higher-ordered network, and disassembly factors that prune filaments from these arrays. While other studies have proposed that these diverse networks arise due to their association with specific molecular regulators, our model suggests that these higher-order actin arrays have much more in common than previously thought. Furthermore, our work contributes to the emerging paradigm that in addition to molecular regulation, the dynamics and sizes of cytoskeletal networks are encoded by their geometry (23, 47–49).

Materials and Methods

Plasmids and Yeast Strains. All strains (*SI Appendix*, Table S1) were constructed using standard methods. To integrate the GFP variant (Envy) at the C terminus of the endogenous Bnr1, primers were designed with complementarity to the 3′ end of the GFP^{Envy} cassette and the C-terminal coding region of Bnr1. PCR was used to generate amplicons from the pFA6a-GFP-His3MX template that allow for selection of transformants using media lacking histidine. The parent strain, *cdc28-13^{ts}*, was transformed with PCR products, and transformants were selected by growth on synthetic media lacking histidine. To integrate a mCherry tag at the C terminus of the endogenous Cdc3, the plasmid pBG1533 (Cdc3-mCherry-LEU) was linearized using the restriction enzyme BglII and transformed into the parent strain, *cdc28-13^{ts}; Bnr1-GFP^{Envy}::His3MX*. Transformants were selected by growth on synthetic media lacking leucine.

Induction of Cell Size Changes. To induce increases in cell size, *cdc28-13^{ts}* cells were grown at the permissive temperature (25 °C) overnight in synthetic complete media (SCM), and then, 10 μL of overnight culture was diluted into 5 mL of fresh SCM. Cultures were then shifted to the restrictive temperature (37 °C) for either 4 or 8 h. After this induction, cells were returned to the permissive temperature (25 °C) for 1 h of growth to allow cell polarization and bud growth and then used for imaging experiments.

Quantitative Analysis of Actin Cable Length, Number, and Fluorescence Intensity in Fixed Cells. Strains were grown at 25 °C to mid-log phase (OD_{600} ~ 0.3) in SCM or were first induced for cell size changes as indicated above. Then cells were fixed in 4.4% formaldehyde for 45 min, washed three times in phosphate-buffered saline (1× PBS), and stained with Alexa Fluor 488–phalloidin (Life Technologies) for ≥24 h at 4 °C. Next, cells were washed three times in 1× PBS and imaged in Vectashield mounting media (Vector Laboratories). Three-dimensional (3D) stacks were collected at 0.2 μm intervals on either a Zeiss LSM 880 using Airyscan superresolution imaging equipped with 63× 1.4 Plan-Apochromat Oil objective lens or a Nikon Ti2-E invert confocal microscope equipped with a CSU-W1 SoRa (Yokogawa) and a Prime BSI sCMOS camera (Teledyne Photometrics) controlled by Nikon Imaging Software (NIS) - Elements Advanced Research software using a 100×, 1.45 NA objective. 3D stacks were acquired for the entire height of the cell. Airyscan image processing was performed using Zen Black software (Carl Zeiss), and SoRa image processing was performed using NIS-Elements Advanced Research software (Nikon). Quantification of actin cable length was performed as previously described (50).

To quantify the actin cable number, we generated line scans of phalloidin fluorescence intensity across the approximate equator of the mother cell from background subtracted maximum intensity projection images. Lines were drawn to avoid fluorescence signal intensity associated with actin patches. Actin cables were counted by automated detection of fluorescence peaks from line scan profiles using custom Python scripts. Peaks were only identified as cables if their fluorescence intensity was greater than 20% of the maximum peak intensity within a single line scan.

To quantify the fluorescence intensity along the length of cables, we manually traced individual cables in background subtracted sum intensity projection images, from the bud neck to their terminus in the mother cell. We only included clearly discernable cables that did not intersect with other cables or actin patches. We used these line scans to record the fluorescence intensity at each position along the cable. To compare the fluorescence decay profiles of cables from different cells, the data were imported into custom Python scripts where their fluorescence intensity was normalized and rescaled so that the maximum intensity was equal to one, and the minimum fluorescence value was set to zero. These profiles were fit to a single exponential to measure their decay length.

Simulation Protocol. We used stochastic simulations to simulate the assembly of actin cables based on our two-dimensional model of cable length control. In the simulation, the system is composed of a number of rows (determined by the number of formins, N_f, contributing to cable assembly) in which filaments of length L_f are added. We start these simulations with a row that contains zero filaments (i.e., a single formin that has not assembled any actin filaments) and then follow the trajectory of this row over time. For each step of the simulation, a single filament of length L_f is added to the row, and all other filaments within that row are selected to undergo one of the possible transitions–they are removed from the row or they remain in the row. These transitions are chosen at random based on their relative weight, which is proportional to the rate of the transition. Following these transitions, the system is updated to a new state and another step of the simulation is executed. The time elapsed between simulation steps is determined by the time required for a filament of length L_f to be assembled by the formin at the assembly rate, k_+. This process is independently repeated for each row of the system, based on the number of formins (N_f), and the length of the entire cable is determined as the distance from the initial filament position in the row to the distal end of the longest surviving filament in any row. This process is repeated for long enough time such that the length of the cable reaches steady-state.

Quantification of Bnr1 Bud Neck Fluorescence Intensity. Strains were first induced for cell size changes as indicated above, and the density of each culture was measured using a spectrophotometer. The density of each culture was normalized by adding additional SCM to the culture tube, and equal amounts of cells were harvested by centrifugation. Media were decanted, and cells were resuspended in 50 μL fresh SCM and combined into a single tube and gently mixed. Approximately 5 μL of

the cell suspension mixture was added onto a 1.2% agarose pad (made with SCM), and 3D stacks were collected at 0.2 μm intervals were acquired at room temperature on a Marianas spinning disk confocal system (3I, Inc, Denver, CO), consisting of a Zeiss Observer Z1 microscope equipped with a Yokagawa CSU-X1 spinning disk confocal head, a QuantEM 512SC EMCCD camera, PLAN-APOCHROMAT 100× oil immersion objectives (NA 1.4), and Slidebook software. Images were processed using custom ImageJ macros. Briefly, sum intensity projections were generated, and the Cdc3-mCherry channel was used for segmentation of the bud neck region of each cell. These segmentation masks were used to measure the total fluorescence intensity of Bnr1-GFP^{Envy} for each cell, and the lengths of each cell (i.e., the distance from the bud neck to the rear of the cell) were manually measured.

Data, Materials, and Software Availability. All images are archived at Zenodo (51), and source code is available at GitHub (https://github.com/shanemc11/2D-CableModel). Data are available in the main text or in *SI Appendix*.

ACKNOWLEDGMENTS. We thank Sam Walcott, Luis Vidali, Lishibanya Mohapatra, and Julie Theriot for thoughtful comments on the manuscript. This research was supported by an award from the NSF Postdoctoral Research Fellowships in Biology Program to S.G.M. (Grant No. 2010766), a grant from the Simons Foundation (www.simonsfoundation.org/) to J.K., a grant from the NIH to B.L.G. (R35 GM134895), and the Brandeis University NSF Materials Research Science and Engineering Center, grant 2011846.

1. Y.-H.M. Chan, W. F. Marshall, How cells know the size of their organelles. *Science* **337**, 1186–1189 (2012).
2. A. Haupt, N. Minc, How cells sense their own shape–Mechanisms to probe cell geometry and their implications in cellular organization and function. *J. Cell Sci.* **131**, jcs214015 (2018).
3. S. Reber, N. W. Goehring, Intracellular scaling mechanisms. *Cold Spring Harb. Perspect. Biol.* **7**, a019067 (2015), 10.1101/cshperspect.a019067.
4. L. Mohapatra, B. L. Goode, P. Jelenkovic, R. Phillips, J. Kondev, Design principles of length control of cytoskeletal structures. *Annu. Rev. Biophys.* **45**, 85–116 (2016).
5. N. W. Goehring, A. A. Hyman, Organelle growth control through limiting pools of cytoplasmic components. *Curr. Biol.* **22**, R330–R339 (2012).
6. G. Greenan *et al.*, Centrosome size sets mitotic spindle length in Caenorhabditis elegans embryos. *Curr. Biol.* **20**, 353–358 (2010).
7. W. F. Marshall, H. Qin, M. R. Brenni, J. L. Rosenbaum, Flagellar length control system: Testing a simple model based on intraflagellar transport and turnover. *Mol. Biol. Cell* **16**, 270–278 (2005).
8. S. G. McInally, J. Kondev, S. C. Dawson, Length-dependent disassembly maintains four different flagellar lengths in Giardia. *Elife* **8**, e48694 (2019).
9. L. Mohapatra, B. L. Goode, J. Kondev, Antenna mechanism of length control of actin cables. *PLoS Comput. Biol.* **11**, e1004160 (2015).
10. V. Varga, C. Leduc, V. Bormuth, S. Diez, J. Howard, Kinesin-8 motors act cooperatively to mediate length-dependent microtubule depolymerization. *Cell* **138**, 1174–1183 (2009).
11. D. S. Banerjee, S. Banerjee, Size regulation of multiple organelles competing for a limiting subunit pool. *PLoS Comput. Biol.* **18**, e1010253 (2022).
12. J. B. Moseley, B. L. Goode, The yeast actin cytoskeleton: From cellular function to biochemical mechanism. *Microbiol. Mol. Biol. Rev.* **70**, 605–645 (2006).
13. S. M. Buttery, S. Yoshida, D. Pellman, Yeast formins Bni1 and Bnr1 utilize different modes of cortical interaction during the assembly of actin cables^{DV}. *Mol. Biol. Cell* **18**, 13 (2007).
14. M. Evangelista, D. Pruyne, D. C. Amberg, C. Boone, A. Bretscher, Formins direct Arp2/3-independent actin filament assembly to polarize cell growth in yeast. *Nat. Cell Biol.* **4**, 32–41 (2002).
15. D. Pruyne, L. Gao, E. Bi, A. Bretscher, Stable and dynamic axes of polarity use distinct formin isoforms in budding yeast. *Mol. Biol. Cell* **15**, 4971–4989 (2004).
16. A. Bretscher, Polarized growth and organelle segregation in yeast. *J. Cell Biol.* **160**, 811–816 (2003).
17. M. Chesarone, C. J. Gould, J. B. Moseley, B. L. Goode, Displacement of formins from growing barbed ends by Bud14 is critical for actin cable architecture and function. *Dev. Cell* **16**, 292–302 (2009).
18. M. Chesarone-Cataldo *et al.*, The myosin passenger protein Smy1 controls actin cable structure and dynamics by acting as a formin damper. *Dev. Cell* **21**, 217–230 (2011).
19. J. A. Eskin, A. Rankova, A. B. Johnston, S. L. Alioto, B. L. Goode, Common formin-regulating sequences in Smy1 and Bud14 are required for the control of actin cable assembly in vivo. *Mol. Biol. Cell* **27**, 828–837 (2016).
20. S. G. McInally, J. Kondev, B. L. Goode, Scaling of subcellular actin structures with cell length through decelerated growth. *Elife* **10**, e68424 (2021).
21. W. F. Marshall, Cellular length control systems. *Annu. Rev. Cell Dev. Biol.* **20**, 677–693 (2004).
22. T. Kamasaki, R. Arai, M. Osumi, I. Mabuchi, Directionality of F-actin cables changes during the fission yeast cell cycle. *Nat. Cell Biol.* **7**, 916–917 (2005).
23. A. Manhart *et al.*, Quantitative regulation of the dynamic steady state of actin networks. *Elife* **8**, e42413 (2019).
24. P. J. Michalski, A. E. Carlsson, A model actin comet tail disassembling by severing. *Phys. Biol.* **8**, 046003 (2011).
25. P. J. Michalski, A. E. Carlsson, The effects of filament aging and annealing on a model lamellipodium undergoing disassembly by severing. *Phys. Biol.* **7**, 026004 (2010).
26. H. Y. Kueh, W. M. Brieher, T. J. Mitchison, Quantitative analysis of actin turnover in listeria comet tails: Evidence for catastrophic filament turnover. *Biophys. J.* **99**, 2153–2162 (2010).
27. N. Ofer, A. Mogilner, K. Keren, Actin disassembly clock determines shape and speed of lamellipodial fragments. *Proc. Natl. Acad. Sci. U.S.A.* **108**, 20394–20399 (2011).
28. J. A. Theriot, T. J. Mitchison, L. G. Tilney, D. A. Portnoy, The rate of actin-based motility of intracellular Listeria monocytogenes equals the rate of actin polymerization. *Nature* **357**, 257–260 (1992).
29. C. A. H. Allard, F. Decker, O. D. Weiner, J. E. Toettcher, B. R. Graziano, A size-invariant bud-duration timer enables robustness in yeast cell size control. *PLoS One* **13**, e0209301 (2018).
30. G. E. Neurohr *et al.*, Excessive cell growth causes cytoplasm dilution and contributes to senescence. *Cell* **176**, 1083–1097.e18 (2019).
31. P. Jorgensen, Systematic identification of pathways that couple cell growth and division in yeast. *Science* **297**, 395–400 (2002).
32. L. W. Pollard, M. V. Garabedian, S. L. Alioto, S. Shekhar, B. L. Goode, Genetically inspired in vitro reconstitution of *Saccharomyces cerevisiae* actin cables from seven purified proteins. *Mol. Biol. Cell* **31**, 335–347 (2020).
33. J. F. Amatruda, J. F. Cannon, K. Tatchell, C. Hug, J. A. Cooper, Disruption of the actin cytoskeleton in yeast capping protein mutants. *Nature* **344**, 352–354 (1990).
34. A. C. E. Wirshing, S. G. Rodriguez, B. L. Goode, Evolutionary tuning of barbed end competition allows simultaneous construction of architecturally distinct actin structures. *J. Cell Biol.* **222**, e202209105 (2023).
35. S. M. Buttery, K. Kono, E. Stokasimov, D. Pellman, Regulation of the formin Bnr1 by septins anda MARK/Par1-family septin-associated kinase. *Mol. Biol. Cell* **23**, 4041–4053 (2012).
36. L. Gao, W. Liu, A. Bretscher, The yeast formin Bnr1p Has two localization regions that show spatially and temporally distinct association with septin structures. *Mol. Biol. Cell* **21**, 1253–1262 (2010).
37. M. V. Garabedian *et al.*, A septin-Hof1 scaffold at the yeast bud neck binds and organizes actin cables. *Mol. Biol. Cell* **31**, 1988–2001 (2020), 10.1091/mbc.E19-12-0693.
38. K. Ong, C. Wloka, S. Okada, T. Svitkina, E. Bi, Architecture and dynamic remodelling of the septin cytoskeleton during the cell cycle. *Nat. Commun.* **5**, 5698 (2014).
39. I. V. Kukhtevich, N. Lohrberg, F. Padovani, R. Schneider, K. M. Schmoller, Cell size sets the diameter of the budding yeast contractile ring. *Nat. Commun.* **11**, 2952 (2020).
40. M. V. Garabedian *et al.*, Integrated control of formin-mediated actin assembly by a stationary inhibitor and a mobile activator. *J. Cell Biol.* **217**, 3512–3530 (2018).
41. B. R. Graziano *et al.*, The F-BAR protein Hof1 tunes formin activity to sculpt actin cables during polarized growth. *Mol. Biol. Cell* **25**, 1730–1743 (2014).
42. L. M. F. de Godoy *et al.*, Comprehensive mass-spectrometry-based proteome quantification of haploid versus diploid yeast. *Nature* **455**, 1251–1254 (2008).
43. H. A. Crissman, J. A. Steinkamp, Rapid, simultaneous measurement of DNA, protein, and cell volume in single cells from large mammalian cell populations. *J. Cell Biol.* **59**, 766–771 (1973).
44. M. C. Lanz *et al.*, Increasing cell size remodels the proteome and promotes senescence. *Mol. Cell* **82**, 3255–3269.e8 (2022).
45. C. Brownlee, R. Heald, Importin α partitioning to the plasma membrane regulates intracellular scaling. *Cell* **176**, 805–815.e8 (2019).
46. E. Rieckhoff *et al.*, Spindle scaling is governed by cell boundary regulation of microtubule nucleation. *Curr. Biol.* **30**, 4973–4983.e10 (2020), 10.1016/j.cub.2020.10.093.
47. R. M. Garner, J. A. Theriot, Leading edge maintenance in migrating cells is an emergent property of branched actin network growth. *Elife* **11**, e74389 (2022).
48. A.-C. Reymann *et al.*, Nucleation geometry governs ordered actin networks structures. *Nat. Mater.* **9**, 827–832 (2010).
49. A. Rosario, S. G. McInally, P. R. Jelenkovic, B. L. Goode, J. Kondev Universal length fluctuations of actin structures found in cells. biorxiv [Preprint] (2023). https://doi.org/10.1101/2023.07.27.550898v1 (Accessed 17 October 2023).
50. S. McInally, J. Kondev, B. Goode, Quantitative analysis of actin cable length in yeast. *Bio. Protoc.* **12**, e4402 (2022).
51. S. McInally *et al.*, Data and imaging files for: Length control emerges from cytoskeletal network geometry. Zenodo (2024). 10.5281/zenodo.11192889. Deposited 14 May 2024.